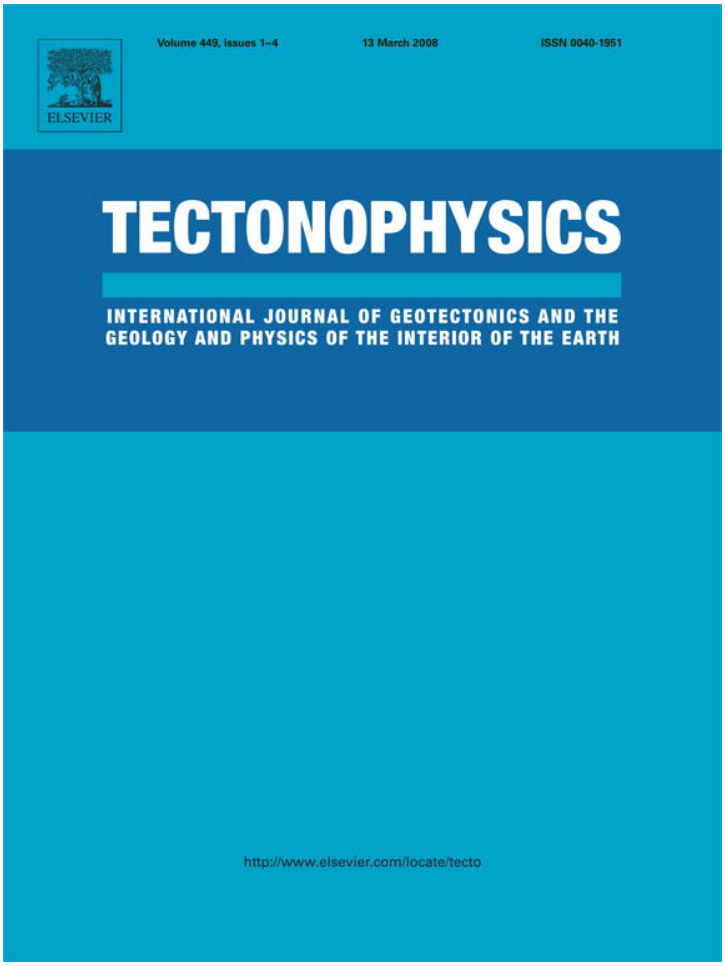

Available online at www.sciencedirect.com
ScienceDirect
Tectonophysics 449 (2008) 120–132
TECTONOPHYSICS
www.elsevier.com/locate/tecto

Talc friction in the temperature range 25°–400 °C: Relevance for Fault-Zone Weakening

Diane E. Moore *, David A. Lockner [1]

U. S. Geological Survey, MS/977, 345 Middlefield Road, Menlo Park, CA 94025 USA

Received 3 July 2007; received in revised form 19 November 2007; accepted 23 November 2007
Available online 3 December 2007

Abstract

Talc is one of the weakest minerals that is associated with fault zones. Triaxial friction experiments conducted on water-saturated talc gouge at room temperature yield values of the coefficient of friction, μ (shear stress, τ/effective normal stress, σ'_N) in the range 0.16–0.23, and μ increases with increasing σ'_N. Talc gouge heated to temperatures of 100°–400 °C is consistently weaker than at room temperature, and $\mu<0.1$ at slow strain rates in some heated experiments. Talc also is characterized by inherently stable, velocity-strengthening behavior (strength increases with increasing shear rate) at all conditions tested. The low strength of talc is a consequence of its layered crystal structure and, in particular, its very weak interlayer bond. Its hydrophobic character may be responsible for the relatively small increase in μ with increasing σ'_N at room temperature compared to other sheet silicates.

Talc has a temperature–pressure range of stability that extends from surficial to eclogite-facies conditions, making it of potential significance in a variety of faulting environments. Talc has been identified in exhumed subduction zone thrusts, in fault gouge collected from oceanic transform and detachment faults associated with rift systems, and recently in serpentinite from the central creeping section of the San Andreas fault. Typically, talc crystallized in the active fault zones as a result of the reaction of ultramafic rocks with silica-saturated hydrothermal fluids. This mode of formation of talc is a prime example of a fault-zone weakening process. Because of its velocity-strengthening behavior, talc may play a role in stabilizing slip at depth in subduction zones and in the creeping faults of central and northern California that are associated with ophiolitic rocks.
Published by Elsevier B.V.

Keyword: Fault gouge; Frictional strength; Fault-zone weakening; Talc

1. Introduction

The evidence for a weak San Andreas fault, based initially on the heat-flow investigations of Brune et al. (1969) and Lachenbruch and Sass (1980) and the stress-orientation data of Mount and Suppe (1987) and Zoback et al. (1987), led to a search for possible causes. One way to reduce strength is to localize shear in fault gouge consisting of weak minerals, but the search for a sufficiently weak mineral that is stable at seismogenic depths was initially unsuccessful. Room-temperature experiments on the serpentine mineral chrysotile (Reinen et al., 1994; Reinen and Tullis, 1995) suggested that it would be a possible candidate, but chrysotile was found to become considerably stronger at temperatures above ≈150 °C (Moore et al., 1996b, 1997, 2004). Water-saturated smectite clays such as montmorillonite are very weak at low stresses at room temperature, but strength increases substantially with increasing effective stress (Morrow et al., 1992; see review by Moore and Lockner, 2007b). In addition, montmorillonite is not stable at temperatures above 100–150 °C (e.g., Abercrombie et al., 1994), reacting to form the stronger clay mineral illite.

Our recent investigations of the room-temperature frictional strengths of layer-structure minerals (Morrow et al., 2000; Moore and Lockner, 2004) showed that talc is as weak as montmorillonite at 100 MPa effective normal stress. Unlike montmorillonite, talc is stable over a wide range of temperature–pressure conditions ranging from surficial environments to

* Corresponding author. Tel.: +1 650 329 4825; fax: +1 650 329 5143.
E-mail addresses: dmoore@usgs.gov (D.E. Moore), dlockner@usgs.gov (D.A. Lockner).
[1] Tel.: +1 650 329 4826; fax: +1 650 329 5143.

0040-1951/$ - see front matter. Published by Elsevier B.V.
doi:10.1016/j.tecto.2007.11.039

Table 1
Summary of talc friction experiments

Experiment Name	Temp. (°C)	σ_N (MPa)	Pp (MPa)	σ'_N (MPa)	Forcing Blocks	Gouge[a]	Comments
25°/100DW	25	100/110	Dry/10	100	Sandst/gran[b]	C	0.5 μm/s (Moore and Lockner, 2004)
25°/100D	25	100	Dry	100	Sandst/gran[b]	C	0.5 μm/s (Moore and Lockner, 2004)
25°/300DW	25	300/310	Dry/10	300	Sandst/gran[b]	C	0.5 μm/s
25°/25	25	40	15	25	Sandst/gran[b]	B	Velocity steps; internal load cell
25°/50	25	80	30	50	Sandst/gran[b]	B	Velocity steps; internal load cell
100°/100D	100	100	Dry	100	Granodiorite	B	0.5 μm/s
100°/50	100	80	30	50	Granodiorite	B	Velocity steps
100°/100	100	150	50	100	Serpentinite	B	Velocity steps
100°/150	100	200	50	150	Granodiorite	B	Velocity steps
200°/100D	200	100	Dry	100	Serpentinite	B	0.5 μm/s
200°/50	200	80	30	50	Serpentinite	B	Velocity steps
200°/100	200	150	50	100	Serpentinite	B	Velocity steps
200°/150	200	200	50	150	Serpentinite	B	Velocity steps
300°/100D	300	100	Dry	100	Granodiorite	B	0.5 μm/s
300°/50	300	80	30	50	Granodiorite	B	Velocity steps
300°/100	300	150	50	100	Serpentinite	B	Velocity steps
300°/150	300	200	50	150	Granodiorite	B	Velocity steps
400°/100D	400	100	Dry	100	Granodiorite	B	0.5 μm/s
400°/50	400	80	30	50	Serpentinite	B	Velocity steps
400°/≈111[c]	400	150[c]	50	100[c]	Serpentinite	B	Velocity steps
400°/150	400	200	50	150	Granodiorite	B	Velocity steps

[a] B=talc schist, Balmat, NY; C=commercial talc powder.
[b] Top piece sandstone, bottom piece granodiorite (Westerly granite).
[c] Run at constant 150 MPa confining pressure, 100 MPa effective pressure; $\sigma'_N \approx 111$ MPa at axial displacements >0.75 mm.

the coesite-eclogite facies (see review by Evans and Guggenheim, 1988). The maximum thermal stability of talc is ≈800 °C, at 1–2 GPa (Chernosky et al., 1985; Jenkins et al., 1991), and the maximum pressure at which talc is stable is ≈5 GPa, at 710 °C (Pawley and Wood, 1995). The effects of changes in temperature, stress, and sliding velocity on the frictional strength of talc were investigated in this study, to determine whether or not talc would remain weak at depth in fault zones. The results demonstrate that talc becomes even weaker when heated; it is weak enough to satisfy the apparent limitations on the strength of the San Andreas fault and it is characterized by stable shear at all temperature–pressure–velocity conditions tested. These findings may have important implications for the behavior of active faults such as subduction thrusts and the central creeping section of the San Andreas fault.

2. Experimental procedures

2.1. Talc gouge materials

Experiments conducted specifically for this study (Table 1) used talc separated from talc-rich schists of the Gouverneur mining district near Balmat, New York (obtained from Ward's Natural Science). The schists occur as lenses and sheets in sheared Grenville Series marbles (Ross et al., 1968), and most of the talc formed as a result of metasomatic reactions between quartzite and dolomite. The coarse-grained, white, transparent talc has nearly end-member composition; the principal substitution is ≈0.5 wt.% F for hydroxyl ion $(OH)^-$ (Ross et al., 1968).

Samples of the talc schist were crushed to small pieces to facilitate removal of the carbonate minerals that are the principal accessory phases in the schist. The talc separate was ground by hand and passed through a 90-μm sieve to produce an essentially monomineralic, synthetic fault gouge. An X-ray diffraction pattern of the prepared gouge contained no peaks attributable to minerals other than talc. The talc grains in the gouge (Fig. 1) are substantially smaller than the 90-μm sieve openings, with a maximum length of ≈30 μm. Numerous 20-μm long pieces are present, and sizes range down to <1 μm.

Previous room-temperature experiments on talc (Moore and Lockner, 2004) that are included in this study (Table 1) used a commercial talc powder of end-member composition obtained from Fisher Scientific.

2.2. Room-temperature experiments

Experimental procedures for the room-temperature experiments are described by Moore and Lockner (2004), and the

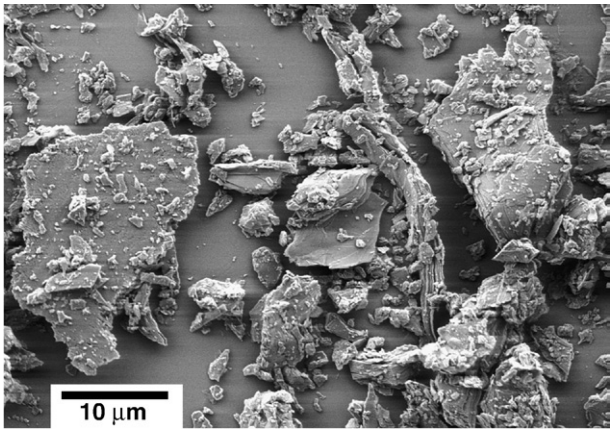

Fig. 1. Secondary-electron SEM image of talc-gouge starting material.

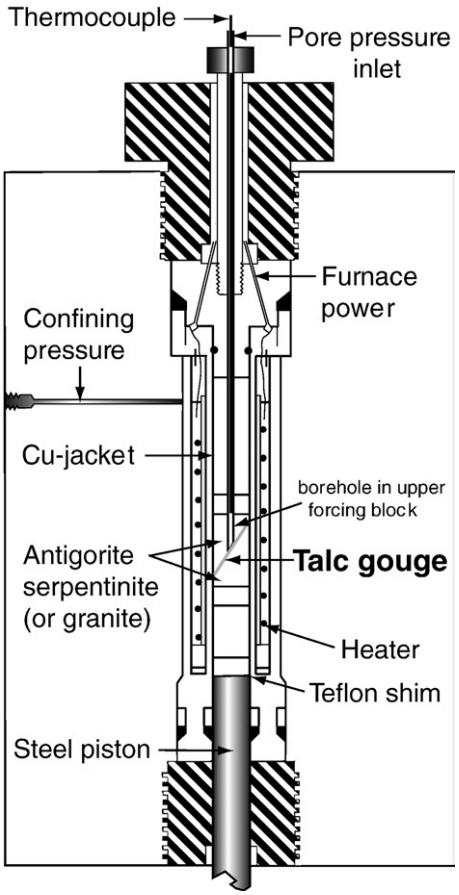

Fig. 2. Furnace assembly for heated experiments in triaxial machine.

room-temperature sample assembly is illustrated in Fig. 2 of that paper. The room-temperature samples consist of a 1-mm thick layer of gouge placed along a 30° sawcut in a 25.4-mm diameter rock cylinder. The lower forcing block was prepared from Westerly granite and the top one from Berea sandstone. The high-porosity sandstone provides good access of the pore fluid to the gouge layer. Low-permeability granite was used for the lower forcing block, to prevent the possibility that pore fluids might become trapped in a more porous material beneath the low-permeability phyllosilicate gouge and generate excess fluid pressures due to poroelastic effects during shear (e.g., Morrow et al., 1992, 2000). Both sawcut surfaces were ground with 240-grit SiC.

The procedures for the two room-temperature tests on the Balmat talc gouge (Table 1) differ from the other three in the use of an internal load cell to measure axial load and in testing a range of sliding velocities. The internal load cell eliminates the corrections for seal friction and the velocity dependence of seal friction that are required when an external load cell is used to measure axial stress. Other corrections are the same as for the previous room-temperature experiments; they include the strength of the polyurethane jacket and a correction for the changes in contact area along the sliding surface. In addition, 0.4 MPa is added to the normal stress on the sawcut that balances the horizontal shear resistance on the greased teflon shim placed between the sample and the loading piston. The latter correction represents an average strength of the interface; our data suggest that the strength term for greased teflon on steel has only minor sensitivity to the normal stress.

2.3. Heated experiments

The experiments at elevated temperatures used the furnace assembly illustrated in Fig. 2. The main differences between the heated and room-temperature experiments stem from the size limitations imposed by the furnace and the use of annealed copper rather than polyurethane jackets. The 19.1-mm diameter samples that are required to fit into the furnace restrict the amount of offset than can be achieved in an experiment. Initial gouge-layer thickness was 1 mm, as at room temperature. The rock used for the forcing blocks was either antigorite serpentinite or granodiorite (Table 1). Talc can coexist with either serpentine- or quartz-bearing rocks, and the granodiorite forcing blocks seemed to allow more shear displacement before jacket failure than did the serpentinite ones. A borehole for pore-fluid entry was drilled into the upper forcing block; a short steel tube inserted into the borehole minimized the extrusion of gouge into the borehole. The gouge-filled cylinder was placed in an annealed copper jacket between titanium carbide end plugs and Lucalox insulators. The narrow space between the jacketed assembly and the furnace (Fig. 2) was loosely packed with boron nitride, which is a good thermal and poor electrical conductor. To produce a dry gouge for some experiments, the jacketed sample was dried overnight (about 22 h) at 120 °C in a vacuum oven to remove the water adsorbed onto crystal surfaces. Transfer of the oven-dried sample to the pressure vessel was completed as quickly as possible.

Once in the pressure vessel, confining pressure was applied first to the sample, followed by pore pressure for water-saturated experiments, using deionized water for the pore fluid. The pore-pressure lines were evacuated over the length of the dry experiments. The temperature was then raised to the desired value; temperature was monitored by a thermocouple inserted along the pore-pressure inlet. The experiments were all run at a constant normal stress, which was maintained by means of computer-controlled adjustments to the confining pressure. Axial displacement and differential stress values were approximately zeroed before the beginning of the experiment; slight adjustments were made, as necessary, after the experiment. Axial displacement rates varied between 0.01 and 1.0 μm/s; corresponding displacement rates along the sawcut are ≈15% higher. The internal load cell cannot be used with the furnace assembly, necessitating corrections for seal friction. The absolute value of seal friction was subtracted from the load cell reading before sample contact. Because seal friction is a function of confining pressure, an additional correction was applied during the experiment to account for the continuing adjustments to confining pressure to maintain a constant normal stress. The velocity dependence of seal friction was checked at the beginning of each experiment by means of a velocity step that was made before the piston contacted the sample. The correction to the normal stress for lateral slip on a greased teflon shim between the sample and forcing piston is +0.7 MPa.

The shear resistance of the annealed copper jacket is removed from the total shear stress after the experiment. The extreme weakness of talc required a more precise knowledge of jacket strength corrections than earlier studies on stronger samples. Revisions to the Cu-jacket strength corrections, resulting from a new series of calibration tests, are detailed in the Appendix. The effect of this change on previously published data at elevated temperatures is minimal. Other than talc, the weakest mineral that has been tested in the copper jackets is chrysotile, and the lowest values of μ (≈ 0.1) reported by Moore et al. (1996b, 1997, 2004) increase by 0.02–0.03 with application of the revised jacket corrections. The changes do not affect any of the conclusions of those studies.

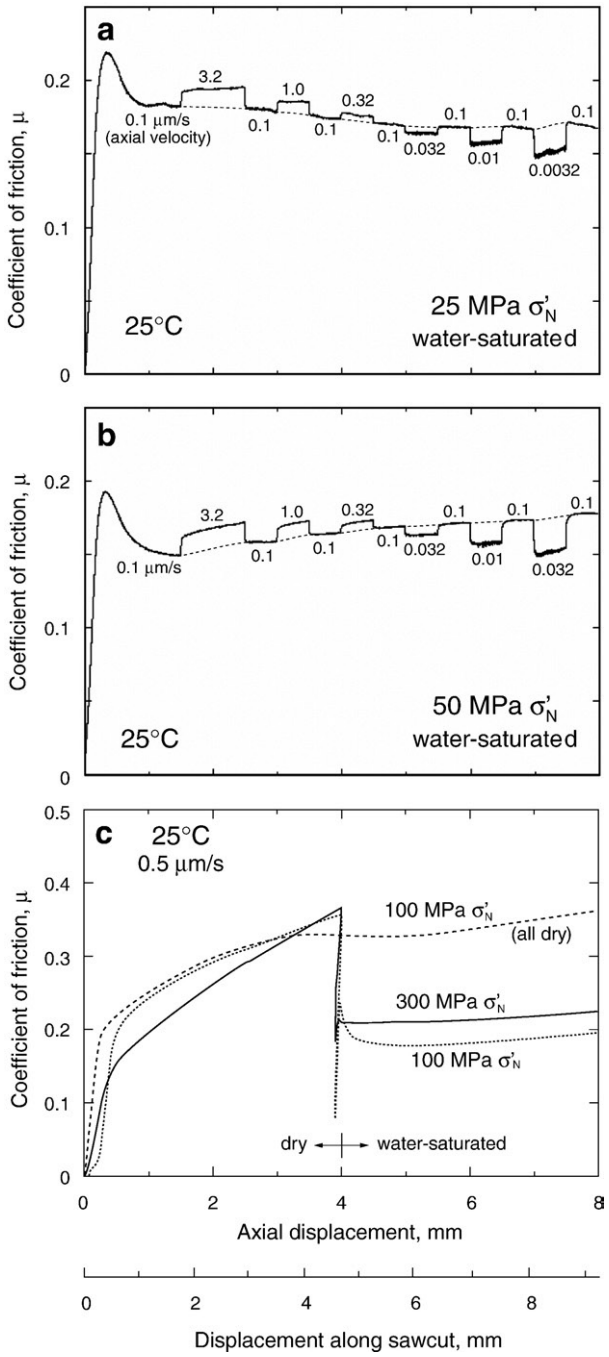

Fig. 3. Room-temperature talc friction experiments. Water-saturated, velocity-stepping experiments were run at a) 25 MPa σ'_N and b) 50 MPa σ'_N. c) All-dry and dry/wet experiments at 100 and 300 MPa σ'_N; pore pressure was 10 MPa in wet portions of the experiments.

3. Results

3.1. Strength experiments

The five room-temperature experiments conducted on talc are plotted in Fig. 3. For the two velocity-stepping experiments (Fig. 3a, b), 0.1 μm/s was used as the "reference" velocity, such that the axial velocity alternated between 0.1 μm/s and the other rates. This procedure was adopted to account for any displacement-dependent changes in frictional resistance. Both water-saturated experiments (Fig. 3a, b) are characterized by an initial peak in μ at small displacements followed by a drop to the residual value of μ. For every velocity step in the two experiments, the measured strength was higher at the higher velocity. The velocity dependence of shear strength is discussed in more detail below.

Thoroughly dried gouges of sheet-silicate minerals are considerably stronger than their water-saturated equivalents (Moore and Lockner, 2004). The sample labelled "all dry" in Fig. 3c was run dry for the entire experiment; the other two experiments were run dry for the first 4 mm, then shearing was halted while the sample was saturated to 10 MPa fluid pressure. Shearing was resumed after about an hour, to allow for equilibration of the pore fluid pressure in the sample (Moore and Lockner, 2004). Strength decreased by ≈40–45% with the addition of water at constant effective normal stress. At $\sigma'_N = 100$ MPa, $\mu \approx 0.20$ for water-saturated talc, and μ increases by ≈0.03 with an increase in σ'_N from 100 to 300 MPa.

The experiments conducted on water-saturated talc at elevated temperatures (Fig. 4) also reach the residual strength at <1 mm displacement. At displacements >0.5 mm, $\mu \leq 0.15$ in nearly all experiments, with minimum values at 300 °C. The coefficient of friction is lowest during the 0.01 μm/s velocity step in all experiments that reached that step. At 100 °C the talc sample tested at $\sigma'_N = 50$ MPa is weakest, whereas at 400 °C the sample tested at $\sigma'_N = 50$ MPa is the strongest. The results at 200° (Fig. 4b) and at 300 °C (Fig. 4c) closely overlap.

Several of the talc samples showed abrupt, minor shifts in strength in the absence of imposed changes in experimental conditions. For example, during the 400°/50 MPa experiment (Fig. 4d), a transient increase of $\mu \approx 0.006$ occurred between 1.10 and 1.25 mm axial displacement. Similarly, μ shifted upwards at 2.15 mm then downwards at ≈2.6 mm axial displacement during the 100°/50 MPa experiment (Fig. 4a). Such variations may accompany transient or permanent changes in gouge texture, such as the formation and removal of an obstruction on a shear surface. Nearly all of these fluctuations in strength occurred in the experiments at $\sigma'_N = 50$ MPa.

The dry experiments summarized in Fig. 5 include the dry portion of the 100 MPa dry/wet talc experiment (Fig. 3c) for comparison. Strength-displacement trends are similar for all the samples, and all of the heated experiments plot below the one

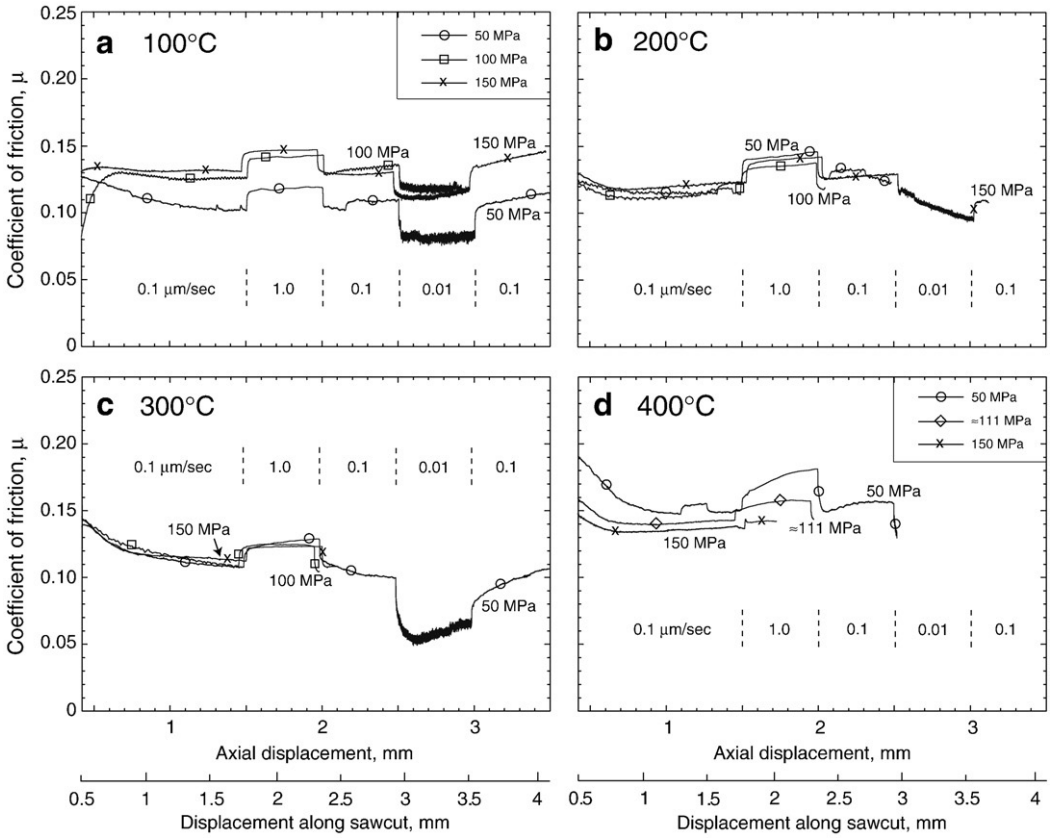

Fig. 4. Summary of heated, velocity-stepping experiments on water-saturated talc gouge at a) 100 °C, b) 200 °C, c) 300 °C, and d) 400 °C.

conducted at room temperature. Dry strength decreases with increasing temperature to 300 °C, much as observed for water-saturated experiments, and then recovers somewhat at 400 °C. The 400 °C values of μ are shifted downwards from the room-temperature values by ≈0.05. Over the restricted displacement interval, all of the samples are characterized by continuous strain-hardening; strength is expected to level off at somewhat higher displacements, as was the case for the all-dry room-temperature talc sample in Fig. 3c.

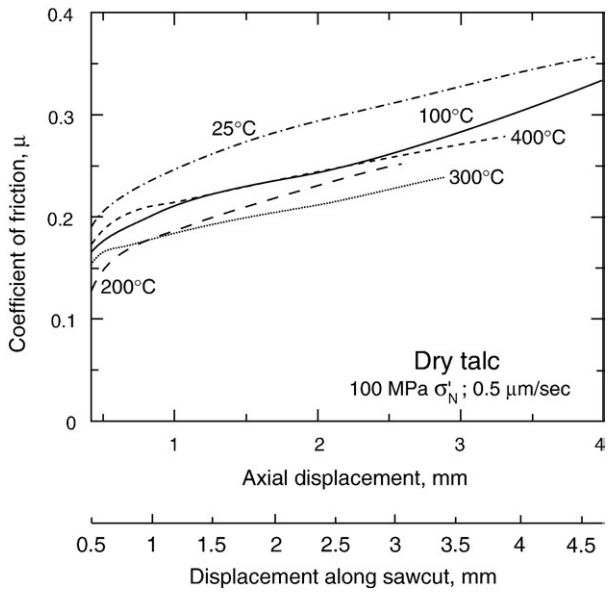

Fig. 5. Friction experiments on oven-dried talc at constant axial velocity of 0.5 µm/s.

3.2. Velocity dependence of shear strength

The sliding rate sensitivity of shear strength is represented by the change in "steady state" coefficient of friction, $\Delta\mu_{ss}$, resulting from a logarithmic change in velocity: $\Delta\mu_{ss}/\Delta\ln V$. For the heated experiments, which did not use an internal load cell, a correction $\Delta\mu_{seal}/\Delta\ln V = 0.0006$ was subtracted from the measured values, to account for the velocity dependence of seal friction. Blanpied et al. (1995) reported no discernible rate dependence of Cu-jacket strength, and they estimated an upper bound of 0.0002 for the contribution of the jackets to $\Delta\mu_{ss}/\Delta\ln V$.

As mentioned previously, the alternation of velocity steps at 0.1 µm/s with steps at other rates establishes a reference strength-displacement trend (e.g., Fig. 3a, b) that reduces the problem of separating velocity- and displacement-dependent effects on μ. To determine $\Delta\mu_{ss}/\Delta\ln V$, the maximum and minimum difference in μ between a given velocity step and the 0.1 µm/s reference line was measured. Determinations of maxima and minima take into account the fluctuations in strength that occurred during some velocity steps (Fig. 4). The average of the two values was reported as $\Delta\mu_{ss}/\Delta\ln V$ and the range in values as the error estimate (Table 2). Jackets failed after small displacements in several of the heated experiments (Fig. 4), with the result that some velocity steps are missing.

Table 2
Velocity dependence of μ for talc

Sample Name (see Table 1)	logV	$\Delta\mu_{ss}/\Delta\ln V$	Error $\Delta\mu/\Delta\ln V$
25°/25	−1.75	+0.0051	±0.0007
	−1.50	+0.0046	±0.0006
	−1.25	+0.0040	±0.0007
	−0.75	+0.0033	±0.0008
	−0.50	+0.0035	±0.0010
	−0.25	+0.0035	±0.0010
25°/50	−1.75	+0.0066	±0.0007
	−1.50	+0.0064	±0.0007
	−1.25	+0.0058	±0.0009
	−0.75	+0.0050	±0.0010
	−0.50	+0.0041	±0.0003
	−0.25	+0.0039	±0.0005
100°/50	−0.50	+0.0058	±0.0015
	−1.50	+0.0097	±0.0026
100°/100	−0.50	+0.0054	±0.0005
	−1.50	+0.0081	±0.0021
100°/150	−0.50	+0.0067	±0.0006
	−1.50	+0.0073	±0.0014
200°/50	−0.50	+0.0075	±0.0012
200°/100	−0.50	+0.0074	±0.0016
200°/150	−0.50	+0.0060	±0.0005
	−1.50	+0.0055	±0.0011
300°/50	−0.50	+0.0077	±0.0024
	−1.50	+0.0114	±0.0031
300°/100	−0.50	+0.0074	±0.0009
300°/150	−0.50	+0.0047	±0.0012
400°/50	−0.50	+0.0077	±0.0034
400°/100	−0.50	+0.0042	±0.0017
400°/150	−0.50	+0.0011	±0.0004

All of the values of $\Delta\mu_{ss}/\Delta\ln V$ are positive, that is, strength increases with increasing shearing rate. All of the values are larger than their accompanying error estimates. Talc thus is characterized by velocity strengthening behavior – strength increases with increasing velocity – over the range of velocities measured. The smallest change in μ was measured in the 400°/150 MPa experiment. Overall, $\Delta\mu_{ss}/\Delta\ln V$ becomes larger at slower velocities. This is best illustrated by the two room-temperature experiments, which have the widest range of velocities. In most of the heated experiments, the slower velocity step yielded the larger value of $\Delta\mu_{ss}/\Delta\ln V$, as well. At 25 °C, the change in strength for a given velocity step was always greater at 50 MPa than at 25 MPa; however, the opposite relationship holds for most of the heated samples.

In most cases a change in sliding rate resulted in an immediate change in shear resistance without a time- or slip-dependent evolution in strength. That is, in the relation $\Delta\mu_{ss}/\Delta\ln V=(a-b)$, the b term is almost always zero. The characteristic sliding distance to reach steady state after a velocity step, D_c, is also nearly always zero. Similar behavior is observed for many wet clays and is phenomenologically equivalent to a nonlinear fluid viscosity or plasticity. Velocity parameter a has been modelled as a thermally activated rate process (e.g., Nakatani, 2001; see review by Paterson and Wong, 2005). Briscoe and Evans (1982) also derived a stress-aided, thermally activated model for shear characterized by velocity-strengthening behavior between organic monolayers deposited on muscovite cleavage faces.

3.3. Petrography

To prepare thin sections from some of the tested samples, the jacketed samples were epoxied before being sliced along the

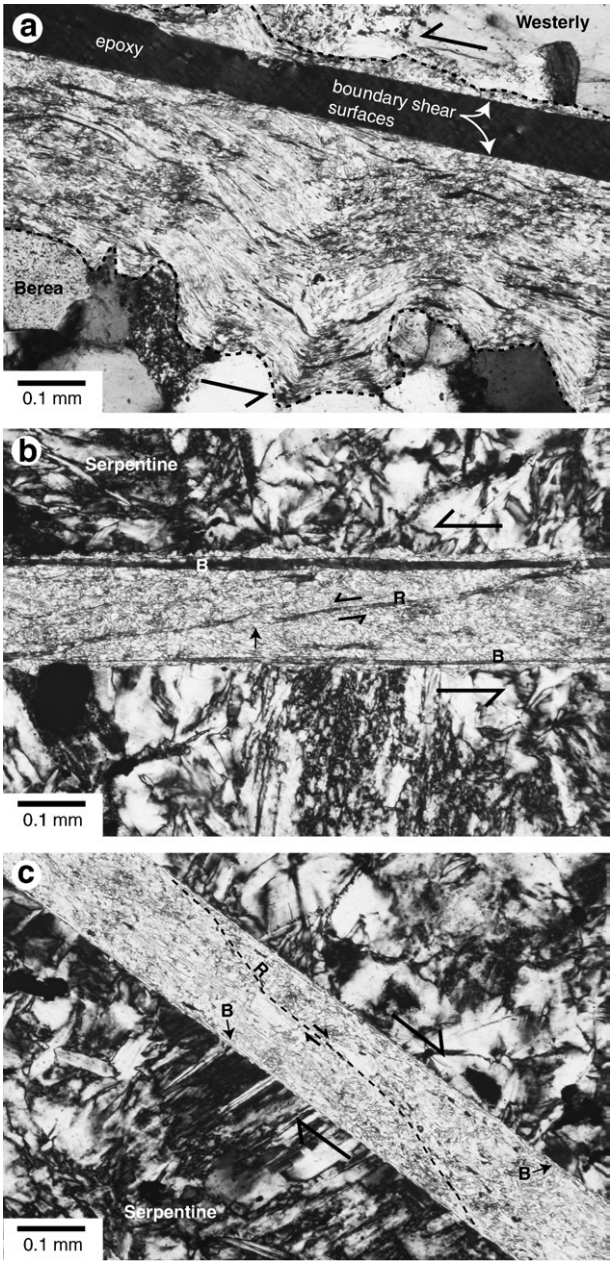

Fig. 6. Photomicrographs of talc gouge layers seen under crossed polarizers in thin section. Pairs of large arrows indicate the shear sense of the gouge layer, and pairs of small arrows the displacement direction of subsidiary R shears within the gouge. a) Room-temperature experiment at 25 MPa σ'_N. Shear is localized near the smoother granite surface. The gouge layers separated along the shear surface; the black band is epoxy. Dashed lines mark the gouge-forcing block boundaries. On the sandstone side, the gouge has squeezed into depressions, where sand grains had been plucked from the surface when the sawcut was made, and they form a folded and kinked surface that has not been modified by shear. b) Talc sample tested at 300 °C and 100 MPa σ'_N in a serpentinite cylinder. Positions of relatively straight boundary shears (B) and more irregular R shears are marked by epoxy. c) Talc gouge from 200 °C experiment at 100 MPa σ'_N. The path of an irregular R shear is marked by a dashed line; it flattens out in the middle of the gouge layer near some larger talc grains.

length of the cylinder and perpendicular to the sawcut (Fig. 6). The jackets were removed from the other samples for preliminary examination with a stereomicroscope; small oriented fragments of gouge were then mounted on plugs for SEM analysis (Fig. 7). The gouge layer undergoes considerable compaction upon application of the confining pressure; all of the sectioned samples were ≤ 0.3 mm thick, with a minimum of ≈ 0.15 mm (Fig. 6). Such a large amount of compaction is not uncommon for pure sheet-silicate gouges. In comparison, quartzofeldspathic gouges tested in the triaxial apparatus typically compact from 1 mm to ≈ 0.6 mm at 100–250 MPa confining pressure. The talc-gouge slurry applied to the sawcut surface was smoothed to an even thickness but not compacted, and randomness in orientation of the platelets in the gouge layer can lead to very high porosities. Compaction of the gouge upon application of the confining pressure, followed by further compaction and reorientation during shear, dramatically lowers porosity and gouge thickness. The gouge layer from the experiment at 25 MPa σ'_N, (Fig. 6a) is thicker than those from experiments at 100 MPa σ'_N (Fig. 6b, c). Even with such thin

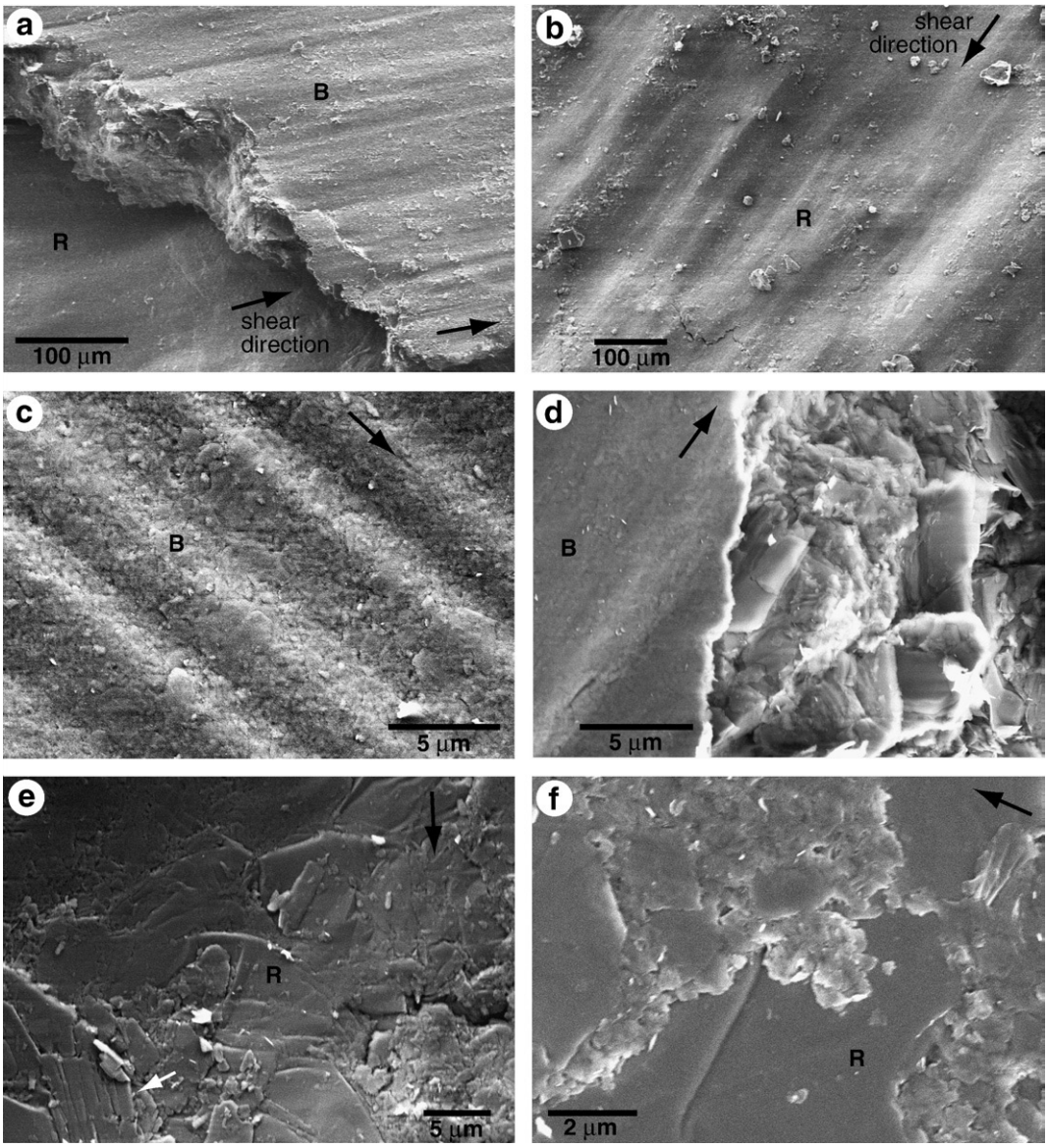

Fig. 7. Secondary-electron SEM images of boundary and R shear surfaces developed in talc gouge. Each photo looks down on one face of the shear; arrows indicate the slip direction of the surface under view. a) Approach of an R shear to a boundary shear surface, 300 °C test at 50 MPa σ'_N. The boundary shear is more regularly striated and the striations more closely spaced than on the R shear. The thin wedge of talc gouge trapped between the two shears is more highly compacted and has a stronger fabric than the gouge farther from the shears. b) Room-temperature sample, 50 MPa σ'_N. Low-power view of a relatively lumpy R shear. R shears also have a looser and less organized appearance than the boundary shears. c) Closer view of boundary shear surface, 100 °C test at 100 MPa σ'_N. Boundary shears typically show considerably more grain-size reduction than R shears (compare with e, f). Most grain size reduction probably occurs during the initial shear displacement, corresponding to the early maxima in μ in Fig. 4. d) Cross-sectional view of boundary shear and gouge within the layer; 100 °C test at 100 MPa σ'_N. The boundary shear is more cohesive and more densely packed than the rest of the gouge. e) R shear surface from 400 °C talc experiment at 100 MPa σ'_N. The platy talc grains slightly overlap, so that they make a small angle to the overall shear surface. The talc grain marked by the white arrow looks corroded, but other grains on the shear do not show obvious dissolution or recrystallization features. f) In-lens secondary-electron image of R-shear surface from 300 °C dry experiment at 100 MPa σ_N.

samples, the shear in the talc layer is further localized to very narrow boundary and Riedel (R) shears.

The boundary shears are positioned close to but not directly against the forcing-block surface (Fig. 6); minimum separation is ≈7 μm. Shear of the room-temperature sample tested at 25 MPa σ'_N was localized along a single boundary shear close to the smoother granite forcing block (Fig. 6a). On the other side the gouge has been pushed into depressions in the sandstone, giving it a folded appearance. Smaller depressions in the Westerly sawcut surface contain similarly folded gouge. Riedel shears tend to be more irregular than the boundary shears; the one in Fig. 6b is relatively straight but has a stepover in the middle of the gouge layer, whereas the orientation of the R shear in Fig. 6c varies across the gouge layer. Such geometric irregularities may be responsible for some of the minor variations in strength, described previously. On average, the R shears are oriented at 10–13° to the boundary shears (e.g., Fig. 6b). The platy grains can have almost any orientation within the gouge layer, although orientations subparallel to the shear direction or defining a P fabric are the most common.

The samples removed from the jackets for SEM study separated along the slickensided boundary (Fig. 7a) and R (e.g., Fig. 7b) shear surfaces. Both types of shear are characterized by shiny and striated surfaces, but the boundary shears are regularly striated even at small scales (Fig. 7c), whereas the R shears are considerably more irregular (Fig. 7b). Each side of a given shear is very thin, more cohesive and more closely packed than the rest of the gouge (Fig. 7a, d). The gouge making up the boundary shears appears to be substantially finer-grained than the gouge as a whole (Fig. 7d) and somewhat finer-grained than the talc comprising the R shears (Fig. 7e, f). The dominant feature of all the boundary and R shears (Fig. 7) is the orientation of the (001) cleavage faces of the grains parallel to the shear planes. The rotation of grains and the grain size reduction accompanying shear formation may cause the initial peaks in μ for the water-saturated experiments (see also Moore and Lockner, 2004). Gouge that is wedged between R and boundary shears near their intersections (Fig. 7a) tends to be more compacted and foliated than gouge situated farther from the shears. The R shear in Fig. 7f is from one of the dry, heated experiments; its texture corresponds to those of R shears in the water-saturated samples, in particular with respect to the alignment of the (001) faces parallel to the shears.

There is no evidence that talc was replaced by other minerals during the experiments, but some dissolution of talc in the heated, initially deionized water is likely, at rates and concentrations that will increase with temperature. Recrystallization of talc may have occurred either during an experiment or accompanying the drop in temperature at the end of the experiment. Gouge that had extruded into the borehole in the upper forcing block (Fig. 2) of a sample tested at 400 °C contains small euhedral plates of talc that may be recrystallized grains as well as a few cylinders of silica about 10 μm in diameter. The gouge layer itself is not texturally or mineralogically distinguishable from the dry heated samples (Fig. 7e, f), except for possibly corroded talc crystals such as the one marked by a white arrow on the R shear surface in Fig. 7e. There was no evidence of reaction between the talc gouge and the forcing blocks of either serpentinite or granodiorite, and the use of serpentinite or granodiorite did not affect the development of deformation textures in the gouge layers.

4. Discussion of results

Published friction data on talc are relatively scarce. Horn and Deere (1962) were among the first to document the marked differences in frictional strength between dry and water-saturated sheet silicates. In their experiments they dragged mineral "buttons" over flat surfaces of the same mineral; their talc samples were prepared from talc schists. They reported $\mu=0.36$ for oven-dried talc, $\mu=0.24$ for air-equilibrated talc, and $\mu=0.16$ for water-saturated talc; the latter value is included in Figs. 8 and 9. The dry strengths are essentially the same as those measured by Morrow et al. (2000) and Moore and Lockner (2004). Scruggs et al. (1993) reported $\mu=0.22$ at 25 MPa for a "humid" talc gouge that would roughly correspond to the air-equilibrated talc tested by Horn and Deere (1962). Hickman et al. (1997) and Escartin et al. (2004) deformed solid, polycrystalline talc specimens in triaxial compression experiments at temperatures to 600 °C. Their results show that the low frictional strength of talc persists to temperatures higher than those reached in this study, and that talc remains weaker than other sheet silicates at the higher temperatures.

The frictional properties of talc and of all other sheet-structure minerals are tied to their relatively weak interlayer bonds and the preferred orientation of the platy grains in the boundary and R shears subparallel to the shear direction (Fig. 7). Dry frictional strengths of sheet-structure minerals at room temperature correlate directly to their (001) bond strengths, presumably because shearing through the (001) bonds of most of these minerals requires less energy than other frictional mechanisms (Moore and Lockner, 2004). Adding water reduces the frictional strength of the sheet-structure minerals. Experiments by Israelachvili

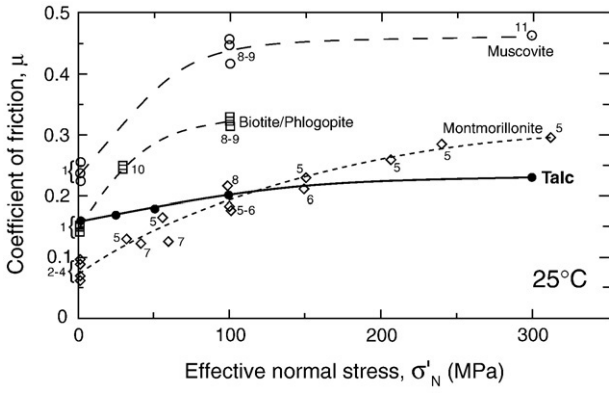

Fig. 8. Room-temperature strengths of some 2:1 sheet silicates as a function of σ'_N. Talc is hydrophobic, whereas the other three minerals are hydrophilic. Other data sources are 1: Horn and Deere (1962); 2–4: Kenney (1967), Lupini et al. (1981), and Maio and Fenelli (1994); 5: Morrow et al. (1992); 6: Moore and Lockner (2007b); 7: Lockner and Tanaka, unpublished data; 8: Morrow et al. (2000); 9: Moore and Lockner (2004); 10: Scruggs and Tullis (1998); and 11: Moore and Lockner, unpublished data. All of the data reported from our laboratory are the values of μ at 8 mm axial displacement.

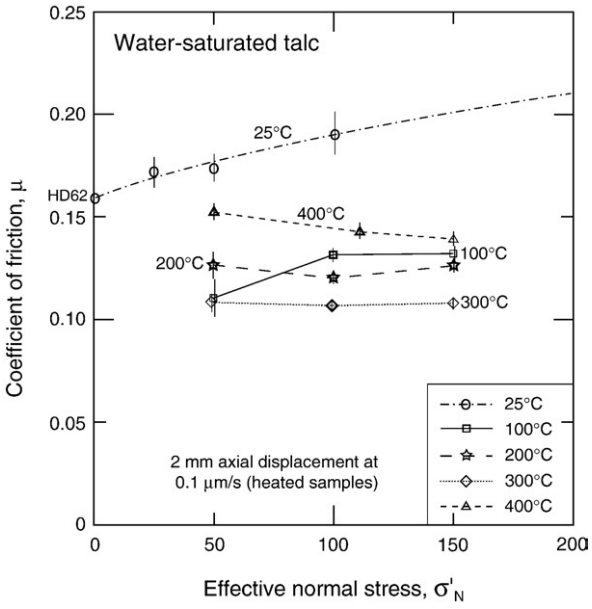

Fig. 9. Summary of the water-saturated talc friction data reported in this study. Bold symbols represent experiments run with serpentinite forcing blocks and plain symbols experiments that used granodiorite. Heated values of μ and room-temperature data at 25 and 50 MPa σ'_N were measured at (or extrapolated to) 2 mm axial displacement at 0.1 μm/s. Room-temperature data at 100 and 300 MPa are also extrapolated back to 2 mm axial displacement for comparison with the other data. The 25 °C data point at low σ'_N is from Horn and Deere (1962). Error bars for closely spaced data points are shifted slightly to improve visibility.

et al. (1988) demonstrated that structured water films form between the cleavage faces of adjacent mica crystals, and the films have a measurable shear strength that increases with decreasing film thickness. These films are weaker than the (001) bonds of the mineral substrate, and shear of a water-saturated gouge composed of platy minerals is concentrated in the water films at the plate surfaces (Moore and Lockner, 2004).

Friction of water-saturated sheet-silicate gouges is more complicated than that of the dry gouges, in part because the crystal structures of the minerals affect the structure and properties of the interfacial water in different ways. An example of this is illustrated in Fig. 8, which compares the normal-stress dependence of μ for some 2:1 sheet silicates at room temperature. The coefficient of friction of each of the four types of 2:1 mineral increases with increasing σ'_N. Such behavior may be a common characteristic of the sheet silicates, because the serpentine minerals, kaolinite, and chlorite show a similar relationship between μ and σ'_N at room temperature. However, the stress dependence of μ is much smaller for talc than for the other 2:1 sheet silicates in Fig. 8; μ of talc increases by 0.06–0.07 between ≈0.1 and 300 MPa, compared to increases in μ of 0.20–0.25 for montmorillonite, biotite/phlogopite, and muscovite over the same range. As a result, talc is stronger than montmorillonite, biotite, and phlogopite at very low normal stresses but weaker than those minerals at 300 MPa.

The principal contributor to the interlayer bonds of the 2:1 sheet silicates is the layer charge. Talc has essentially 0 layer charge, montmorillonite has a layer charge of approximately −0.33 per formula unit, and muscovite, phlogopite, and biotite ideally have layer charges of −1 per formula unit. The lack of a layer charge is the origin of the hydrophobic character of talc; the other minerals in Fig. 8 are hydrophilic (e.g., Giese et al., 1991). All minerals adsorb some water onto their surfaces (van Oss and Giese, 1995), and Edmond and Paterson (1971) reported a weight loss of ≈0.4% for a room-dry talc specimen that was heated at a temperature slightly above 100 °C for an hour. However, hydrophobic talc should adsorb less water than the hydrophilic minerals, and recent molecular dynamics models of the interaction of water with the surfaces of talc and muscovite (Wang et al., 2006) illustrate why this is true. In their model of the muscovite-water system, water molecule dipoles in the first water layer above the cleavage face are oriented perpendicular to the surface (Wang et al., 2006), an orientation that is favorable for attracting additional layers of the polar water molecules. They also found that the hydration energy of water adsorbed at the muscovite surface is at a minimum, increasing gradually to the bulk value with increasing thickness of the water film. Cantrell and Ewing (2001) determined from spectroscopic investigations that a cleavage surface of muscovite takes on the equivalent of 5 monolayers of water at saturation, consistent with the hydration energies calculated by Wang et al. (2006). Similarly, Ormerod and Newman (1983) determined that water sorption on the external surfaces of montmorillonite should reach the equivalent of ≈6 monolayers at saturation. At low normal stresses, relatively thick water films can be maintained between adjoining cleavage planes of these minerals (e.g., Renard and Ortoleva, 1997), considerably reducing shear strength. The film thickness decreases and its shear strength increases with increasing effective stress.

In contrast, water molecules in the first layer above the talc surface have their dipoles oriented approximately parallel to the (001) face, with the result that these water molecules are bonded more strongly to each other than to the talc surface (Wang et al., 2006). Such an orientation should also limit the attraction of other water molecules to the first water layer. In addition, calculated hydration energy is higher than the bulk water value at the crystal surface (Wang et al., 2006). Consequently, at low effective stresses water films in the hydrophobic talc gouge are likely to be thinner than those in gouges of the hydrophilic minerals, and talc is stronger than some of those minerals at low-stress conditions. The talc gouge will also be less affected by changing effective normal stress than the other minerals in Fig. 8.

The summary of water-saturated talc friction in Fig. 9 is representative of shear at 0.1 μm/s axial velocity (0.115 μm/s shear rate of the gouge layer), for which the most data are available. Strengths will be shifted downwards at lower velocities and upwards at higher velocities. The room-temperature results provide the upper bounds of talc strength. Overall, at a given effective normal stress strength decreases from 25° to 300 °C, and then partially recovers at 400 °C, as described previously. There is no indication that talc strength was affected by the use of serpentinite (bold symbols in Fig. 9) or granodiorite (plain symbols) for the forcing blocks. The strengths of both dry (Fig. 5) and water-saturated talc (Fig. 9) are affected in the same

way by increasing temperature. In contrast to talc, the dry frictional strengths of antigorite and brucite are unaffected by heating to 300 °C (Moore and Lockner, 2007a). The weakening of dry and wet talc between 25° and 300 °C would be consistent with the progressive weakening of the interlayer bond with increasing bond length (e.g., Gibbs et al., 1998), caused by thermal expansion of the talc c* axis (Pawley et al., 1995). Although the net changes in bond length at the PT conditions of the experiments are small, the effect on the frictional properties of talc might be noticeable because its strength is already low. However, the increases in both dry and water-saturated strengths between 300° and 400 °C require a different explanation, because the interlayer bonds continue to lengthen over that temperature interval. Further study is needed to understand the varying response of talc to heating.

Although there is some scatter in the data at 50 MPa σ'_N, the overall stress dependence of μ appears to change from a modest positive relation at 25° and 100 °C to a negative one at 400 °C. Additional experiments are needed to test the validity of this possible reversal in behavior, particularly at low effective normal stresses where small changes in shear stress will have a substantial effect on μ. However, the data point at 100 °C/50 MPa was verified in a duplicate experiment that used a lead jacket (see the Appendix). The stress dependence of μ of the sheet-structure mineral brucite, $Mg(OH)_2$, changes from positive to negative between 25° and 400 °C (Moore and Lockner, 2005). The heated brucite gouge samples showed obvious evidence of dissolution and recrystallization accompanying shear (see Fig. 10 of Moore and Lockner, 2007a), and Moore and Lockner (2005) attributed the behavior of brucite at elevated temperatures to solution-transfer processes. If the stress dependence of μ for talc illustrated in Fig. 9 is confirmed, the corroded talc grain in the 400 °C sample shown in Fig. 7e might suggest the activation of a solution-transfer mechanism at higher temperatures in the talc gouge, as well, that is a function of stress. In contrast to brucite and perhaps talc, the coefficient of friction of the serpentine mineral chrysotile increases with increasing σ'_N over the temperature range 25°–280 °C (Moore et al., 2004). To date, few investigations at elevated temperatures of the water-saturated friction of sheet-structure gouges have been conducted, to place these different results in context. Much more research is needed to better understand the full range of water–mineral interactions that can occur during shear of these gouges and the relative importance of different interactions on the frictional properties of a given mineral.

5. Concluding remarks: talc and fault-zone weakening

The major finding of this study is that heated, water-saturated talc gouge is extremely weak and characterized by stable, velocity-strengthening shearing behavior over the range of conditions tested. Talc may be the most important weak mineral in fault zones, because it is stable over a much wider range of temperatures and pressures than other weak minerals such as the smectite clays. Talc is restricted in its occurrence to Mg-rich rocks such as metamorphosed ultramafic rocks of the present-day or former (ophiolites) oceanic lithosphere, but ultramafic rocks are intimately involved in the faulting at active plate margins. Talc is a constituent of subduction thrust faults (e.g., Peacock, 1987; Bebout and Barton, 2002) and of oceanic fracture zones (d'Orazio et al., 2004) and detachment faults (Kopf, 2001; Roller et al., 2001) that are associated with slow spreading ridges (see review by Boschi et al., 2006). In addition, talc was recently discovered in the creeping section of the San Andreas fault (Moore and Rymer, 2007) – a continental plate-boundary transform fault – where it cuts ophiolitic rocks at depth. Talc may therefore play a much larger role in faulting than its overall abundance would initially suggest.

The development of talc-rich shears in active faults is a major fault-zone weakening mechanism. Simple hydration of orthopyroxene during metamorphism yields talc, but an extra source of silica is needed to produce talc in metamorphosed dunite and olivine-rich peridotite because the Si/Mg ratio of talc is higher than that of olivine. One way to achieve this is to mix ultramafic rocks with more siliceous rock types. Such mixing has been documented at the slab-mantle interface in exhumed subduction zones (e.g., Bebout and Barton, 2002; Spaggiari et al., 2002). More commonly, Si-saturated hydrothermal fluids provide the additional silica needed for talc to crystallize. In subduction zones, dewatering of the subducting slab releases large amounts of silica-saturated fluids into the mantle wedge above the subduction thrust fault. At temperatures below ≈550 °C, initial hydration of the mantle wedge produces serpentine±brucite. Over time, the continued migration of Si-charged fluids into the serpentinized ultramafic rocks first causes the conversion of any brucite present to serpentine, followed by the replacement of serpentine minerals by talc (Manning, 1995). In such cases, the fault-zone weakening process occurs in two stages as dry ultramafic rock is initially replaced by weaker serpentine minerals and the serpentine replaced, in turn, by even weaker talc. The maximum depth at which talc is stable in the mantle wedge above the subducting slab or in subducted oceanic lithosphere will vary with the temperature profile of the subduction zone.

In a similar fashion, focused flow of seawater-derived hydrothermal fluids in detachment faults near oceanic spreading centers leads to serpentinization and subsequent talc formation at T < 500 °C (e.g., Boschi et al., 2006). Boschi et al. (2006) emphasized the importance of the weak sheet-silicate minerals, particularly talc, in localizing shear and focussing fluid flow along the narrow, long-lived detachment faults.

As noted in the Introduction, we initiated friction experiments on sheet-structure minerals at hydrothermal conditions in an attempt to explain the apparent weakness of the San Andreas fault. Recent modelling of heat-flow measurements (d'Alessio et al., 2006) and stress-orientation data (Chéry et al., 2004) suggest that $\mu = 0.1–0.2$ in the central creeping section of the San Andreas fault, where there is no recourse to dynamic weakening mechanisms accompanying major earthquakes. As demonstrated in this study, talc could satisfy the strength limitations and explain the aseismic slip of the creeping section. Serpentinite was identified in cuttings (Solum et al., 2006) collected during drilling across the active trace of the San Andreas fault at the San Andreas Fault Observatory at Depth (SAFOD), located near the southern end of the creeping section.

Talc has replaced some of the serpentine in the cuttings as a result of reaction with Si-bearing fluids (Moore and Rymer, 2007), the same process that is occurring in subduction zones and oceanic detachment faults. The textures indicate that the talc is forming at the present time in the fault. The talc-bearing cuttings come from a depth of ≈3 km, where the temperature is ≈112 °C (Williams et al., 2006). The abundances of both serpentinite and talc in the SAFOD cuttings are very small, but the amount of serpentinite entrained in the fault might be expected to increase with decreasing distance from its source at depth. The talc-forming reaction might also be enhanced at greater depths, where temperatures are higher and the dissolved silica content of migrating groundwater is substantially greater. Talc is stable relative to serpentine+quartz over the range of thermal stability of serpentine (e.g., Evans and Guggenheim, 1988). The discovery of talc-bearing serpentinite in the active trace thus raises the possibility that offset on a talc-lined shear at greater depths may influence the behavior of the central creeping section of the San Andreas fault.

Appendix A

High-pressure deformation experiments typically require some form of jacketing to prevent the confining medium from infiltrating into the sample pore space. For room temperature triaxial tests, common jacketing materials are polymers such as latex, polyolefin, or polyurethane. At elevated temperatures, thin-walled metal jackets (e.g., In, Pb, Cu, Fe) are used for sample isolation and, in some cases (e.g., Au, Ag, Pt) for minimizing reactivity with internal pore fluids. For our high-temperature experiments, the standard jacketing is 0.38 mm-thick annealed copper tube (1083 °C melting point). At room temperature, these jackets provide shear resistance equivalent to nearly 10 MPa shear stress on a 30° sawcut sample. The jackets become weaker with increasing temperature until, by ≈400 °C, jacket strength is essentially zero (Higgs, 1981). Therefore, jacket strength corrections can become important for modest temperature experiments, especially for low-strength materials such as talc when tested at low effective normal stress.

We have carried out an extensive series of tests to determine relevant jacket strength corrections. Initial tests included standardized strength measurements for copper jackets of different thicknesses (Blanpied et al., 1995). In that calibration series, the samples consisted of thin sheets of greased teflon placed between 30° inclined surfaces of polished steel driving blocks. Jacket shear strength was modeled by an initial yield stress and a linear strain hardening term. For example, the equivalent shear strength of the jackets at 100 °C, as used by Blanpied et al. (1995), was

$$\tau_{100\ ^\circ C} = 9.2 + 1.80\mathrm{dz} \tag{A1}$$

where stress is in MPa and axial shortening, dz, is in mm. Blanpied et al. (1995) found no discernible rate dependence of Cu-jacket strength. The Blanpied et al. (1995) corrections were applied to friction tests of relatively strong crushed granite gouge as well as weaker serpentinite gouge samples (Moore et al., 1996a).

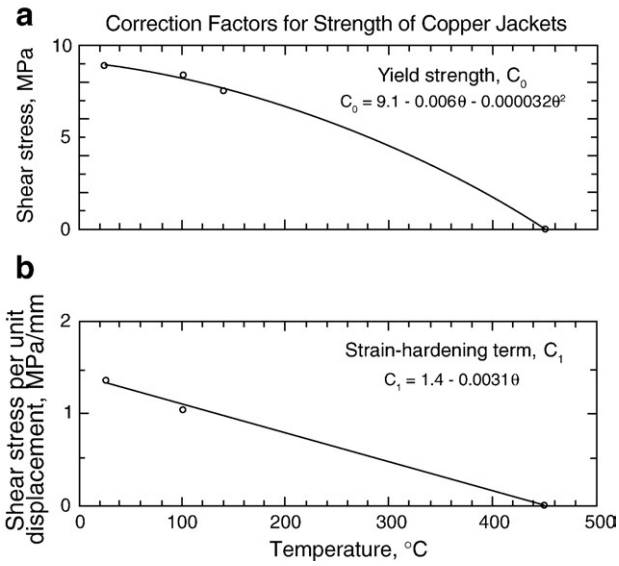

Fig. A1. Revised correction factors for the strength of copper jackets with 0.38 mm wall thickness; a) yield strength. A quadratic equation provides a better fit to the yield-strength data than a straight line and is consistent with the temperature-dependence of copper strength reported by Higgs (1981); b) strain-hardening term. The copper jacket is assumed to reach 0 strength at 450 °C.

In the talc experiments reported here, the samples have unusually low strength and place a more stringent demand on the accuracy of the jacket strength corrections. A main concern was the determination of the yield stress of the annealed copper jackets, because past estimates depended on subtraction of the shear strength of the teflon-on-steel sample (estimated to be approximately 2 MPa). We have now completed an additional set of calibration tests consisting of wafers of indium on steel or granite (shear strength estimated to be approximately 1 MPa), with both polyurethane and lead jackets, at confining pressures ≥20 MPa. Lead (328 °C melting point) is an excellent jacketing material for tests at temperatures up to about 300 °C due to its low strength and high ductility. Incorporating this most recent round of calibrations has led to the temperature-dependent copper jacket corrections shown in Fig. A1. Both the yield stress and strain-hardening terms were assumed to drop to zero at 450 °C. Tests conducted in the temperature range 25–150 °C indicate that the yield stress is better fit by a quadratic than by a linear weakening term. As used in this paper, the temperature-dependent shear strength of annealed, 0.38 mm-wall copper jackets is approximated by

$$\begin{array}{ll} \tau_{\mathrm{jacket}}[\mathrm{MPa}] = C_0(\theta) + C_1(\theta)\mathrm{dz} & 20\ ^\circ C < \theta < 450\ ^\circ C \\ \tau_{\mathrm{jacket}} = 0 & \theta > 450\ ^\circ C \end{array} \tag{A2}$$

with

$$C_0 = 9.1 - 0.006\theta - 0.000032\theta^2$$
$$C_1 = 1.4 - 0.0031\theta$$

These corrections are applicable between 0.5 and 4 mm axial displacement. As an example, our improved copper jacket correction at 100 °C, as used in this paper, is

$$\tau_{100\ ^\circ C} = 8.2 + 1.09\mathrm{dz} \tag{A3}$$

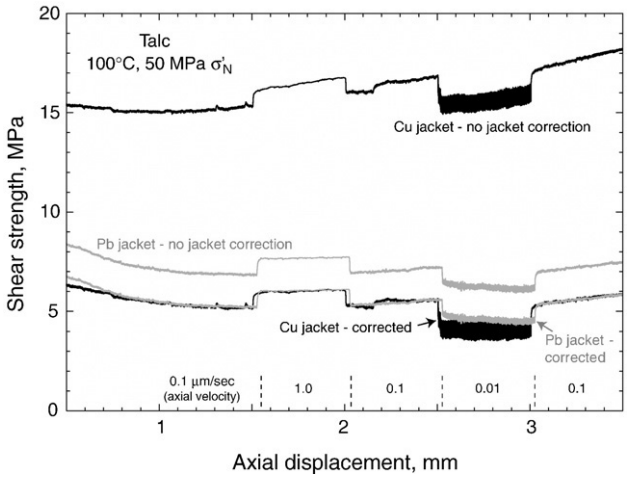

Fig. A2. Results of friction experiments on talc gouge at 100 °C using lead and copper jackets. The yield strength for the copper jacket at 100 °C, estimated from experiments on indium/granite samples, was adjusted to bring the strength data into correspondence with the results of the lead-jacket experiment.

A comparison of Eqs. (A1) and (A3) shows that corrections used by Blanpied et al. (1995) were too large by as much as 4 MPa at 100 °C and 4 mm displacement. For an experiment at 100 MPa normal stress, this results in a 0.04 error in coefficient of friction.

Copper jacket corrections are most problematic in the 100°–200 °C range. In an effort to validate the corrections that were used we conducted two experiments on talc gouge at 100 °C and 50 MPa effective normal stress (Fig. A2). One experiment used a standard 0.38 mm-thick Cu jacket and the second a 1 mm-thick Pb jacket. Lead jackets were tested separately using both indium and teflon wafers to determine yield stress (1.2 MPa) and strain hardening rate (essentially zero). Apparent (uncorrected) shear strength at 2 mm displacement for the copper-jacketed and lead-jacketed samples were 15.5 and 6.5 MPa, respectively (Fig. A2). Applying the jacket corrections resulted in an adjusted shear strength of 5.4 MPa for both experiments. Although the corrected copper-jacketed results appear satisfactory, future tests at temperatures below 250 °C will be carried out with lead or indium jackets where possible.

References

Abercrombie, H.J., Hutcheon, I.E., Bloch, J.D., de Caritat, P., 1994. Silica activity and the smectite–illite reaction. Geology 22, 539–542.

Bebout, G.E., Barton, M.D., 2002. Tectonic and metasomatic mixing in a high-T, subduction-zone mélange — insights into the geochemical evolution of the slab–mantle interface. Chem. Geol. 187, 79–106.

Blanpied, M.L., Lockner, D.A., Byerlee, J.D., 1995. Frictional slip of granite at hydrothermal conditions. J. Geophys. Res. 100, 13,045–13,064.

Boschi, C., Früh-Green, G.L., Escartin, J., 2006. Occurrence and significance of serpentinite-hosted, talc- and amphibole-rich fault rocks in modern oceanic settings and ophiolite complexes: An overview. Ofioliti 31, 129–140.

Briscoe, B.J., Evans, D.C.B., 1982. The shear properties of Langmuir–Blodgett layers. Proc. R. Soc. Lond., A 380, 389–407.

Brune, J.N., Henyey, T.L., Roy, R.F., 1969. Heat flow, stress and rate of slip along the San Andreas fault, California. J. Geophys. Res. 74, 3821–3827.

Cantrell, W., Ewing, G.E., 2001. Thin film water on muscovite mica. J. Phys. Chem., B 105, 5434–5439.

Chernosky Jr., J.V., Day, H.W., Caruso, L.J., 1985. Equilibria in the system $MgO–SiO_2–H_2O$: Experimental determination of the stability of Mg-anthophyllite. Am. Mineral. 70, 223–236.

Chéry, J., Zoback, M.D., Hickman, S., 2004. A mechanical model of the San Andreas fault and SAFOD pilot hole stress measurements. Geophys. Res. Lett. 31, L15S13. doi:10.1029/2004GL019521.

d'Alessio, M.A., Williams, C.F., Bürgmann, R., 2006. Frictional strength heterogeneity and surface heat flow: Implications for the strength of the creeping San Andreas fault. J. Geophys. Res. 111, B05410. doi:10.1029/2005JB003780.

d'Orazio, M., Boschi, C., Brunelli, D., 2004. Talc-rich hydrothermal rocks from the St. Paul and Conrad fracture zones in the Atlantic Ocean. Eur. J. Mineral. 16, 73–83.

Edmond, J.M., Paterson, M.S., 1971. Strength of solid pressure media and implications for high pressure apparatus. Contrib. Mineral. Petrol. 30, 141–160.

Escartin, J., Hirth, G., Evans, B., 2004. Rheology of talc: Consequences for subduction processes and the localization of deformation. Eos Trans. AGU 85 (47), S51B–0415 (Fall Meet. Suppl., Abstract).

Evans, B.W., Guggenheim, S., 1988. Talc, pyrophyllite, and related minerals. In: Bailey, S.W. (Ed.), Hydrous Phyllosilicates (exclusive of micas). Rev. Mineral., vol. 19, pp. 225–294.

Gibbs, G.V., Hill, F.C., Boisen, M.B., Downs, R.T., 1998. Power law relationships between bond length, bond strength and electron density distributions. Phys. Chem. Miner. 25, 585–590.

Giese, R.F., Costanzo, P.M., van Oss, C.J., 1991. The surface free energies of talc and pyrophyllite. Phys. Chem. Miner. 17, 611–616.

Hickman, J.B., Zhurina, E.N., Kronenberg, A.K., 1997. Deformation of talc and pyrophyllite: Disruption of van der Waals bonds and comparisons with calculated interlayer forces. Eos Trans. AGU 78 (46), F724 (Fall Meet. Suppl.).

Higgs, N.G., 1981. Mechanical properties of ultrafine quartz, chlorite, and bentonite in environments appropriate to upper-crustal earthquakes. Ph. D. dissertation, Texas A & M University, College Station, Tx, 267 pp.

Horn, H.M., Deere, D.U., 1962. Frictional characteristics of minerals. Géotechnique 12, 319–335.

Israelachvili, J.N., McGuiggan, P.M., Homola, A.M., 1988. Dynamic properties of molecularly thin liquid films. Science 240, 189–191.

Jenkins, D.M., Holland, T.J.B., Clare, A.K., 1991. Experimental determination of the pressure–temperature stability field and thermochemical properties of synthetic tremolite. Am. Mineral. 76, 458–469.

Kenney, T.C., 1967. The influence of mineral composition on the residual strength of natural soils. Proceedings of the Geotechnical Conference on Shear Strength Properties of Natural Soils and Rocks, Oslo, pp. 123–129.

Kopf, A., 2001. Permeability variation across an active low-angle detachment fault, western Woodlark Basin (ODP Leg 180), and its implication for fault activation. In: Holdsworth, R.E., Strachan, R.A., MagLoughlin, J.F., Knipe, R.J. (Eds.), The Nature and Tectonic Significance of Fault Zone Weakening. Geol. Soc. London Spec. Pub., vol. 186, pp. 23–41.

Lachenbruch, A.H., Sass, J.H., 1980. Heat flow and energetics of the San Andreas fault zone. J. Geophys. Res. 85, 6185–6223.

Lupini, J.F., Skinner, A.E., Vaughan, P.R., 1981. The drained residual strength of cohesive soils. Géotechnique 31, 181–213.

Maio, C.Di, Fenelli, G.B., 1994. Residual strength of kaolinite and bentonite: the influence of their constituent pore fluid. Géotechnique 44, 217–226.

Manning, C.E., 1995. Phase-equilibrium controls on SiO_2 metasomatism by aqueous fluid in subduction zones: Reaction at constant pressure and temperature. Int. Geol. Rev. 37, 1039–1073.

Moore, D.E., Lockner, D.A., 2004. Crystallographic controls on the frictional behavior of dry and water-saturated sheet structure minerals. J. Geophys. Res. 109, B03401. doi:10.1029/2003JB002582.

Moore, D.E., Lockner, D.A., 2005. Solution-transfer processes and the frictional strength of heated brucite. Eos Trans. AGU 86, T21B–0484 (Fall Meet. Suppl., Abstract).

Moore, D.E., Lockner, D.A., 2007a. Comparative deformation behavior of minerals in serpentinized ultramafic rock: Application to the slab–mantle interface in subduction zones. Int. Geol. Rev. 49, 401–415.

Moore, D.E., Lockner, D.A., 2007b. Friction of the smectite clay montmorillonite: a review and interpretation of data. In: Dixon, T.H., Moore, J.C.

(Eds.), The Seismogenic Zone of Subduction Thrust Faults. MARGINS Theoretical and Experimental Earth Science Ser., vol. 2, pp. 317–345.

Moore, D.E., Rymer, M.J., 2007. Talc, serpentinite, and the creeping section of the San Andreas fault. Nature 448, 795–797.

Moore, D.E., Lockner, D.A., Summers, R., Byerlee, J.D., Ma, S., 1996a. Sample characterizations and strength measurements of serpentinite gouges. U. S. Geol. Surv. Open File Report 96–702, p. 88.

Moore, D.E., Lockner, D.A., Summers, R., Ma, S., Byerlee, J.D., 1996b. Strength of chrysotile–serpentinite gouge under hydrothermal conditions: can it explain a weak San Andreas fault? Geology 24, 1041–1044.

Moore, D.E., Lockner, D.A., Ma, S., Summers, R., Byerlee, J.D., 1997. Strengths of serpentinite gouges at elevated temperatures. J. Geophys. Res. 102, 14,787–14,801.

Moore, D.E., Lockner, D.A., Tanaka, H., Iwata, K., 2004. The coefficient of friction of chrysotile gouge at seismogenic depths. In: Ernst, W.G. (Ed.), Serpentine and Serpentinites: Mineralogy, Petrology, Geochemistry, Ecology, Geophysics, and Tectonics. Geol. Soc. Am. Internat. Book Ser., vol. 8, pp. 525–538.

Morrow, C.A., Radney, B., Byerlee, J., 1992. Frictional strength and the effective pressure law of montmorillonite and illite clays. In: Evans, B., Wong, T.-F. (Eds.), Fault Mechanisms and Transport Properties of Rocks. Academic, San Diego, CA, pp. 69–88.

Morrow, C.A., Moore, D.E., Lockner, D., 2000. The effect of mineral bond strength and adsorbed water on fault gouge frictional strength. Geophys. Res. Lett. 27, 815–818.

Mount, V.S., Suppe, J., 1987. State of stress near the San Andreas fault: implications for wrench tectonics. Geology 15, 1143–1146.

Nakatani, M., 2001. Conceptual and physical clarification of rate and state friction: frictional sliding as a thermally activated rheology. J. Geophys. Res. 106, 13,347–13,380.

Ormerod, E.C., Newman, A.C.D., 1983. Water sorption on Ca-saturated clays: II. Internal and external surfaces of montmorillonite. Clay Miner. 18, 289–299.

Paterson, M.S., Wong, T.-F., 2005. Experimental Rock Deformation — The Brittle Field. Springer, New York, NY. 347 pp.

Pawley, A.R., Wood, B.J., 1995. The high-pressure stability of talc and 10 Å phase: potential storage sites for H_2O in subduction zones. Am. Mineral. 80, 998–1003.

Pawley, A.R., Redfern, S.A.T., Wood, B.J., 1995. Thermal expansivities and compressibilities of hydrous phases in the system $MgO–SiO_2–H_2O$: talc, phase A, and 10-Å phase. Contrib. Mineral. Petrol. 122, 301–307.

Peacock, S.M., 1987. Serpentinization and infiltration metasomatism in the Trinity peridotite, Klamath province, northern California: implications for subduction zones. Contrib. Mineral. Petrol. 95, 55–70.

Reinen, L.A., Tullis, T.E., 1995. Microstructural evidence for strain localization and distributed strain in serpentine friction experiments. Eos Trans. AGU 76 (46), F560 (Fall Meet. Suppl.).

Reinen, L.A., Weeks, J.D., Tullis, T.E., 1994. The frictional behavior of lizardite and antigorite serpentinites: experiments, constitutive models, and implications for natural faults. Pure Appl. Geophys. 143, 317–358.

Renard, F., Ortoleva, P., 1997. Water films at grain–grain contacts: Debye–Hückel, osmotic model of stress, salinity, and mineralogy dependence. Geochim. Cosmochim. Acta 61, 1963–1970.

Roller, S., Behrmann, J.H., Kopf, A., 2001. Deformation fabrics of faulted rocks, and some syntectonic stress estimates from the active Woodlark Basin detachment zone. In: Wilson, R.C.L., Whitmarsh, R.B., Taylor, B., Froitzheim, N. (Eds.), Non-Volcanic Rifting of Continental Margins: A Comparison of Evidence from Land and Sea. Geol. Soc. London Spec. Pub., vol. 187, pp. 319–334.

Ross, M., Smith, W.L., Ashton, W.H., 1968. Triclinic talc and associated amphiboles from Gouverneur mining district, New York. Am. Mineral. 53, 751–769.

Scruggs, V.J., Tullis, T.E., 1998. Correlation between velocity dependence of friction and strain localization in large displacement experiments on feldspar, muscovite, and biotite gouge. Tectonophysics 295, 15–40.

Scruggs, V.J., Tullis, T.E., Weeks, J.D., Beeler, N.M., 1993. The role of water in the evolution effect: A comparison between muscovite mica and talc. Eos Trans. AGU 74 (43), F590 (Fall Meet. Suppl.).

Solum, J.G., Hickman, S.H., Lockner, D.A., Moore, D.E., van der Pluijm, B.A., Schleicher, A.M., Evans, J.P., 2006. Mineralogical characterization of protolith and fault rocks from the SAFOD main hole. Geophys. Res. Lett. 33, L21314. doi:10.1029/2006GL027285.

Spaggiari, C.V., Gray, D.R., Foster, D.A., 2002. Blueschist metamorphism during accretion in the Lachlan Orogen, southeastern Australia. J. Metamorph. Geol. 20, 711–726.

van Oss, C.J., Giese, R.F., 1995. The hydrophilicity and hydrophobicity of clay minerals. Clays Clay Miner. 43, 474–477.

Wang, J., Kalinichev, A.G., Kirkpatrick, R.J., 2006. Effect of substrate structure and composition on the structure, dynamics, and energetics of water at mineral surfaces: A molecular dynamics modeling study. Geochim. Cosmochim. Acta 70, 562–582.

Williams, C.F., Grubb, F.V., Galanis, S.P., 2006. Heat flow measurements across the San Andreas fault near Parkfield, California — Preliminary results from SAFOD. Eos Trans. AGU 87 (52), S33B–0241 (Fall Meet. Suppl., Abstract).

Zoback, M.D., Zoback, M.L., Mount, V.S., Suppe, J., Eaton, J.P., Healy, J.H., Oppenheimer, D., Reasenberg, P., Jones, L., Raleigh, C.B., Wong, I.G., Scotti, O., Wentworth, C., 1987. New evidence for the state of stress on the San Andreas fault system. Science 238, 1105–1111.